Available online at www.sciencedirect.com
ScienceDirect
Journal of Power Sources 173 (2007) 310–324
JOURNAL OF POWER SOURCES
www.elsevier.com/locate/jpowsour

Development and experimental validation of a PEM fuel cell dynamic model

Alejandro J. del Real, Alicia Arce, Carlos Bordons *

Departamento de Ingeniería de Sistemas y Automática, Universidad de Sevilla, 41092 Seville, Spain

Received 11 December 2006; received in revised form 23 March 2007; accepted 29 April 2007
Available online 5 May 2007

Abstract

A dynamic model of a 1.2 kW polymer electrolyte membrane (PEM) fuel cell (FC) is developed and validated through a series of experiments. This dynamic model is mostly oriented towards control and operation optimization and can be a useful tool for the design of FC-based systems. In the methodology proposed, theoretical equations are combined with experimental relations, resulting in a semi-empirical formulation. The model assumptions are discussed extensively as the equations are presented. This model contributes to the description of the following areas: fluid dynamics in the gas flow fields and gas diffusion layers (oxygen, hydrogen, liquid water and vapor); thermal dynamics and temperature effects; a novel algorithm to calculate an empirical polarization curve. As a result, this model can predict both steady and transient states (such as flooding and anode purges) due to variable loads, as well as the system start-up. Based on this model, a simulator software package has been developed, which is available upon request. The model parameters have been adjusted specifically for a 1.2 kW Ballard stack, which can be considered a benchmark as it is widely used by research groups worldwide. Finally, the simulated results are compared to experimental data from the Ballard stack, demonstrating the accuracy of the proposed model methodology.

Keywords: PEMFC; Modeling; Dynamic; Temperature; Flooding; Startup

1. Introduction

PEM fuel cells are expected to play an important role in the future energy scenario [1], where they will be used in both automotive and stationary applications, implying that steady-state and transient modes will have to be taken into account. The importance of having an accurate model that predicts the fuel cell behavior is a very important issue. A model not only provides a framework for analyzing the performance of the PEM fuel cell system and its components but it is also valuable in that it can supply the value of internal variables which are difficult to measure, such as the water content inside the flow fields.

There are many PEM fuel cell models in literature. In fact, many fuel cell models have been developed over the past 15 years. Earlier models, such as in Ref. [2], presented an empirical polarization curve based on calculated coefficients, as some recent papers [3] have shown. In Refs. [4–6] an extended equation, with a larger number of parameters was proposed, improving the formulation of the polarization curve dependency on the stack temperature and the hydrogen and oxygen partial pressures. In this paper, an improved equation is presented, which properly models the temperature and reactant partial pressure influence on the curve, as well as the system start up sequence, in conjunction with the dynamic equations of the model. Due to the optimized formulation proposed, a direct geometric-based algorithm can be deduced, which allows a direct equation parameter calculation to be performed using four experimental points and two experimental ratios, improving the off-line and computationally costly iterative method proposed in Ref. [4]. This represents an important improvement since the equation can now be upgraded on-line and be used, for example, in adaptive controllers that could cover the membrane degradation as it ages.

As the polarization curve only includes the steady state by itself, later works have focussed on the fluid dynamics inside the stack, taking transient behavior into account. Bernardi and Vebrunge and Springer et al. [7,8] studied the water flow across the membrane and the variable membrane hydration. Gurski

* Corresponding author. Tel.: +34 954487348; fax: +34 954487340.
E-mail address: bordons@esi.us.es (C. Bordons).

0378-7753/$ – see front matter © 2007 Elsevier B.V. All rights reserved.
doi:10.1016/j.jpowsour.2007.04.066

Nomenclature

a	species activity
A	area (m^2)
c	mole concentration ($mol\,m^{-3}$)
c_p	specific heat capacity ($J\,(kg\,K)^{-1}$)
C	heat capacity ($J\,K^{-1}$)
D	diffusion coefficient ($m^2\,s^{-1}$)
$\langle D \rangle$	effective diffusion coefficient ($m^2\,s^{-1}$)
F	Faraday constant ($C\,mol^{-1}$)
h	mass specific enthalpy ($W\,kg^{-1}$)
h_f^0	mass specific enthalpy of formation ($W\,kg^{-1}$)
$\dot{H}$	enthalpy flow rate (W)
I	current (A)
j	current density ($A\,m^{-2}$)
K	valve coefficient ($kg\,(bar\,s)^{-1}$)
K_h	heat transfer coefficient
m	mass (kg)
$\dot{m}$	mass flow rate ($kg\,s^{-1}$)
M	molar mass ($kg\,mol^{-1}$)
n_d	electro-osmotic drag coefficient
n_{fc}	number of fuel cells
N	molar flux ($mol\,s^{-1}\,m^{-2}$)
p	pressure ($N\,m^{-2}$)
P	power (W)
$\dot{Q}$	heat flow rate (W)
R	ideal gas constant ($J\,(mol\,K)^{-1}$)
s	fraction of liquid water volume to the total volume
s_{im}	level of immobile saturation
S_r	reduced liquid water saturation
t	time (s)
T	temperature (K)
V	volume or voltage (m^3or V)
w	mass fraction
w_r	humidity ratio
x	polarization curve coefficient

Greek letters

α_l	flooding experimental coefficient
α_w	conductivity correction coefficient
γ	volumetric condensation coefficient
δ	thickness of diffusion layer (m)
ε	porosity or emissivity
η	viscosity ($kg\,(m\,s)^{-1}$)
θ_c	contact angle (°)
λ	water content or excess ratio
μ	permeability (m^2)
μ_r	relative permeability ($kg\,mol^{-1}$)
ρ	mass density ($kg\,m^{-3}$)
σ	surface tension or Stefan–Boltzmann constant ($N\,m^{-1}$ or $W\,m^{-2}\,K^{-4}$)
ϕ	relative humidity

Superscripts and subscripts

a	dry air
act	activation
amb	ambient
anch	anode flow channel
anGDL	anode diffusivity gas layer
atm	atmospheric
B	fuel cell stack body
c	capilar
cach	cathode flow channel
caGDL	cathode gas diffusion layer
conc	concentration
conv	convection
cool	coolant
dry	dry
elec	electric
evap	evaporation
fc	fuel cell
forc	forced
g	vapor
gen	generated
H_2	hydrogen
H_2O	water
in	inlet
l	liquid water
ma	moisture air
memb	membrane
nat	natural
N_2	nitrogen
0	initial or reference
ohm	ohmic
out	outlet
O_2	oxygen
p	pore
purge	purge
rad	radiation
react	reaction
sat	saturation
st	fuel cell stack

[9] also considered the reactant flow control. In Ref. [10], the importance of gas hydration was presented, and water transport and its relation with the membrane thickness, while the feeding gases composition was shown in Ref. [11]. Some other models have proposed a multi-dimensional study, such as Refs. [12–14]. More complex approaches in 3D modeling have also been developed [15–19]. Although these contributions are very useful for fuel cell design, they require large computational calculations. Thus, simplified one-dimensional models are more suitable for control purposes, such as the ones presented in Refs. [20–25], and they allow faster simulations and implementations as well. In Ref. [26], both gas diffusion layers (GDLs) and gas flow fields are modeled, considering lumped parameters, dividing each GDL into three control volumes and each flow field into one. The work presented here follows that method, but simplifying the GDLs, considering each one to be a unique control volume and thus reducing the computational cost.

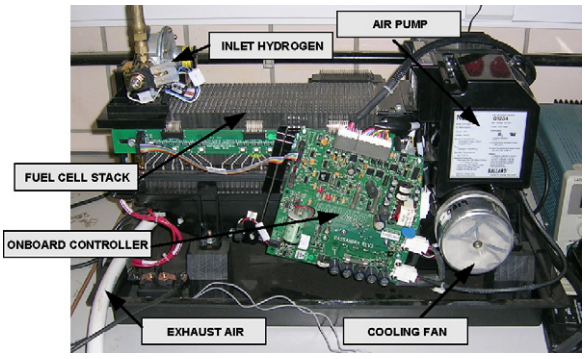

Fig. 1. 1.2 kW Nexa power module.

Concerning thermal dynamics, there are some detailed studies such as in Refs. [27–30]. Wetton [31] proposed an explicit thermal model to analyze the temperature gradient of different layers in the fuel cell stack. Also, Sundaresan [32] presented a very detailed 1D thermal dynamic model. In Ref. [33], all the principal thermal effects are presented, and then the equations are simplified, neglecting the less important coefficients and specifically adapting a water cooled stack. Therefore, this work is a variation, considering here an autohumidified stack with air as coolant.

Notice that many of the existing models neglect the dynamic effects and although some others take these issues into account, there is still a lack of validated experiments. The main contribution of this work is the development of a dynamic model and its validation through real results in a system that is used by many research groups.

2. Test equipment

The experimental data presented in this paper was obtained from a 1.2 kW Ballard PEM fuel cell (Nexa Power Module, see Fig. 1), which is currently being used by many research groups and is representative of the state of the art in PEM technology. The benchmark is equipped with a controller which assumes the control and safety tasks. The stack is composed of 46 cells, each with a 110 cm^2membrane. The system is autohumidified and air-cooled by a small fan. Concerning the hydrogen feeding of the fuel cell, a dead-end mode with flushes was adopted. Also, a PC was used for the acquisition of the measured values and, in order to simulate a variable power demand, the energy produced was delivered to an electronic load.

3. Model description

In the model methodology proposed, theoretical equations are combined with experimental relations, resulting in a semi-empirical formulation. The model assumptions are widely discussed as the equations are presented. Furthermore, it is composed of three main modules: electrochemical static model, fluid-dynamics model and thermal dynamics model. Characteristic fuel cell times are shown in Table 1. As can be seen, electrochemical dynamics can be neglected as they are several orders of magnitude slower than the others, as published in Ref.

Table 1
Time constants of the fuel cell dynamics

Dynamical effect	Characteristic time
Electrochemistry	O (10^{-19})s
Fluid-dynamics	O (10^{-1})s
Temperature	O (10^{2}) s
Content of liquid water	O (10^{2}) s

[34]. Finally, the model, though generalized for standard PEM fuel cell stacks, contains some parameters which depend on the physical dimensions of this system, as well as on several other particular issues, such as membrane characteristics. In this paper, as presented in Section 2, a 1.2 kW Ballard stack has been specifically adapted. Thus, the value of all the parameters are presented in the subsequent sections as well.

3.1. Fluid-dynamics equations

The fluid-dynamics equations consider five control volumes, rather than nine as in the case of Ref. [26], therefore reducing the number of calculations, while still taking into account all of the effects presented in that model. Moreover, additional issues have been included, such as water evaporation and condensation dynamics.

The fluid-dynamics block is composed of five interconnected sub-blocks, which correspond to: the control volumes of the two flow channels; the diffusion gas layers of cathode and anode; the transport of chemical species across the membrane. All of these control volumes are assumed to be at temperatures equal to that of the stack, T_{st}. The signal criteria adopted depends on the direction of the flows, as shown in Fig. 2, where the direction of the arrows corresponds to positive values.

3.1.1. Cathode flow channel

The inlet air flow is supplied by an air pump and conditioned by a humidifier. Thus, the values of the inlet flow $\dot{m}_{cach,in}$, its temperature $T_{cach,in}$ and its relative humidity $\phi_{cach,in}$ must be known. Dry air composition will be assumed to be equal to that of the

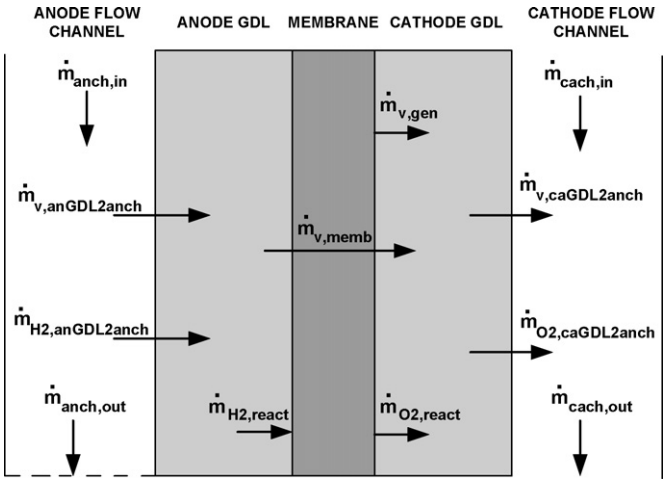

Fig. 2. Signal criteria.

Table 2
Flow channels parameter set

Parameters	Value
δ_{cach}, δ_{anch} (m)	1.5×10^{-3}
n_{fc}	46
A_{fc}^{0} (m^2)	110×10^{-4}
V_{cach}, V_{anch} (m^3)	7.59×10^{-4}
t_{purge} (s)	0.5
$K_{cach,out}$ (kg (bar s)$^{-1}$)	0.01
$K_{anch,out}$ (kg (bar s)$^{-1}$)	0.001
$K_{anch,in}$ (kg (bar s)$^{-1}$)	0.2

atmospheric air. For purpose of simplification, $p_{cach,in} = p_{cach}$. Also, the pressure at the end of the channel equals the atmospheric pressure, $p_{cach,out} = p_{atm}$. The channel is adjacent to the cathode gas diffusion layer, with water exchange $\dot{m}_{l,caGDL2cach}$ and $\dot{m}_{g,caGDL2cach}$ and oxygen exchange $\dot{m}_{O_2,caGDL2cach}$ occurring between them. Nitrogen exchange will be neglected as it is an inert gas. The water flow depends on the difference of concentrations between the flow channel and the GDL control volumes and is calculated in Section 3.1.3. Due to the signal criteria shown in Fig. 2, oxygen flow is negative in the direction of the gas diffusion layer. Furthermore, it equals the oxygen amount which reacts with the hydrogen. This flow is calculated in Section 3.1.3. The differences in oxygen pressure between the cathode flow channel and the cathode gas diffusion layer are negligible, as proven by works like [35], which show that the exchange dynamics due to concentration differences are very low. Finally, the values of all the parameters used in the flow channel sections are presented in Table 2.

The inlet air flow is defined as

$$\dot{m}_{O_2,cach,in} = w_{O_2,cach,in} \frac{1}{1 + w_{r,cach,in}} \dot{m}_{cach,in} \quad (1)$$

$$\dot{m}_{N_2,cach,in} = w_{N_2,cach,in} \frac{1}{1 + w_{r,cach,in}} \dot{m}_{cach,in} \quad (2)$$

$$\dot{m}_{v,cach,in} = \frac{w_{r,cach,in}}{1 + w_{r,cach,in}} \dot{m}_{cach,in} \quad (3)$$

where

$$w_{r,cach,in} = \frac{M_v}{M_a} \frac{\phi_{cach,in} p_{sat}(T_{cach,in})}{p_{cach,in} - \phi_{cach,in} p_{sat}(T_{cach,in})} \quad (4)$$

considering that the dry air mass fraction equals the atmospheric air mass fraction, $w_{O_2,cach,in} = 0.21 M_{O_2} M_a^{-1}$ and $w_{N_2,cach,in} = 0.79 M_{N_2} M_a^{-1}$, where $M_a = 0.21 M_{O_2} + 0.79 M_{N_2} \simeq 0.02885\,kg\,mol^{-1}$.

Applying mass balance to the control volume and assessing the inlet and outlet flows of the channel and the exchange flow between it and the gas diffusion layer result in the equations shown below. Notice that $\dot{m}_{l,cach,in} = 0$, as it can be assumed that no liquid water carried by the inlet air enters the cathode channel and $\dot{m}_{l,caGDL2cach,in} = 0$ because the membrane does not allow liquid water transport, it only allows gas transport. Furthermore, almost all the liquid water condensed inside the cathode channel is dragged by the water exhaust, which results in $dm_{l,cach}/dt = 0$:

$$\frac{dm_{l,cach}}{dt} = \dot{m}_{l,cach,in} - \dot{m}_{l,cach,out} - \dot{m}_{evap,cach} + \dot{m}_{l,caGDL2cach} \quad (5)$$

$$\frac{dm_{v,cach}}{dt} = \dot{m}_{v,cach,in} - \dot{m}_{v,cach,out} + \dot{m}_{v,caGDL2cach} + \dot{m}_{evap,cach} \quad (6)$$

$$\frac{dm_{O_2,cach}}{dt} = \dot{m}_{O_2,cach,in} - \dot{m}_{O_2,cach,out} - \dot{m}_{O_2,caGDL2cach} \quad (7)$$

$$\frac{dm_{N_2,cach}}{dt} = \dot{m}_{N_2,cach,in} - \dot{m}_{N_2,cach,out} \quad (8)$$

$$m_{ma,cach} = m_{O_2,cach} + m_{N_2,cach} + m_{v,cach} \quad (9)$$

In order to describe the evaporation and condensation dynamics inside the channel, the equations proposed in Ref. [36] were used. The $\dot{m}_{evap,cach}$ value is positive when the steam pressure is smaller than the saturation pressure, causing water to evaporate in that case. When the water condenses, the value is negative. Moreover, a logical restriction that would prevent the evaporation of more water than is available must be considered. In this way,

$$\dot{m}_{evap,cach} = \min\left(A_{fc}(p_{sat}(T_{st}) - p_{v,cach}) \sqrt{\frac{M_v}{2\pi R T_{st}}}, \dot{m}_{l,caGDL2cach} \right) \quad (10)$$

Pressures inside the channel are calculated as

$$p_{cach} = p_{O_2,cach} + p_{N_2,cach} + p_{v,cach} \quad (11)$$

$$p_{O_2,cach} = \frac{R T_{st}}{M_{O_2} V_{cach}} m_{O_2,cach} \quad (12)$$

$$p_{N_2,cach} = \frac{R T_{st}}{M_{N_2} V_{cach}} m_{N_2,cach} \quad (13)$$

$$p_{v,cach} = \phi_{cach} p_{sat}(T_{st}) = \frac{R T_{st}}{M_v V_{cach}} m_{v,cach} \quad (14)$$

Supposing that all the liquid water on the surface of the channel is dragged by the air that circulates across the cathode, outlet flows will be:

$$\dot{m}_{ma,cach,out} = K_{cach,out}(p_{cach} - p_{cach,out}) \quad (15)$$

$$\dot{m}_{O_2,cach,out} = \frac{m_{O_2,cach}}{m_{ma,cach}} \dot{m}_{ma,cach,out} \quad (16)$$

$$\dot{m}_{N_2,cach,out} = \frac{m_{N_2,cach}}{m_{ma,cach}} \dot{m}_{ma,cach,out} \quad (17)$$

$$\dot{m}_{v,cach,out} = \frac{m_{v,cach}}{m_{ma,cach}} \dot{m}_{ma,cach,out} \quad (18)$$

$$\dot{m}_{l,cach,out} = \dot{m}_{l,caGDL2cach} - \dot{m}_{evap,cach}. \quad (19)$$

3.1.2. Anode flow channel

The equations that model the anode flow channel are analogous to the ones that model the cathode channel. In this way, applying mass balance, assuming that dry hydrogen enters the channel and taking into account the signal criteria shown in Fig. 2, result in:

$$\frac{dm_{l,anch}}{dt} = -\dot{m}_{l,anGDL2anch} - \dot{m}_{evap,anch} - \dot{m}_{l,anch,out} \quad (20)$$

$$\frac{dm_{v,anch}}{dt} = -\dot{m}_{v,anch,out} - \dot{m}_{v,anGDL2anch} + \dot{m}_{evap,anch} \quad (21)$$

$$\frac{dm_{H_2,anch}}{dt} = \dot{m}_{H_2,anch,in} - \dot{m}_{H_2,anch,out} - \dot{m}_{H_2,anGDL2anch} \quad (22)$$

Water steam and hydrogen partial pressure inside the channel are defined as

$$p_{v,anch} = \frac{RT_{st}}{M_v V_{anch}} m_{v,anch} \quad (23)$$

$$p_{H_2,anch} = \frac{RT_{st}}{M_{H_2} V_{anch}} m_{H_2,anch} \quad (24)$$

Condensation dynamics are calculated as in the cathode side:

$$\dot{m}_{evap,anch} = \min\left(A_{fc}(p_{sat}(T_{st}) - p_{v,anch})\sqrt{\frac{M_v}{2\pi RT_{st}}}, \dot{m}_{l,anGDL2anch}\right) \quad (25)$$

During the experimental time t_{purge}, most liquid water condensed on the surface of the channel is dragged by the purge gas flow, which is calculated as shown below. When the purge valve is closed, $v_{out,open} = 0$ (see Section 3.4.4), being positive when the valve is opened:

$$p_{anch} = p_{v,anch} + p_{H_2,anch} \quad (26)$$

$$\dot{m}_{ma,anch,out} = K_{anch,out} v_{out,open}(p_{anch} - p_{atm}) \quad (27)$$

$$m_{ma,anch} = m_{H_2,anch} + m_{v,anch} \quad (28)$$

$$\dot{m}_{H_2,anch,out} = \frac{m_{H_2,anch}}{m_{ma,anch}} \dot{m}_{ma,anch,out} \quad (29)$$

$$\dot{m}_{v,anch,out} = \frac{m_{v,anch}}{m_{ma,anch}} \dot{m}_{ma,anch,out} \quad (30)$$

$$\dot{m}_{l,anch,out} = \frac{m_{l,anch}}{t_{purge}} \quad \text{if } \dot{m}_{ma,anch,out} > 0. \quad (31)$$

3.1.3. Cathode and anode gas diffusion layers (GDLs)

In Ref. [26], each gas diffusion layer is divided into three control volumes. The equations presented here simplify that study, considering each GDL as a unique control volume. This formulation, although being much simpler and less costly computationally, describes the system behaviour very well. As this is a novel approach, almost all the equations included here present some departure from those presented in the literature. Particularly, the spatial gradients have been linearized, resulting in algebraic equations and thus allowing a simpler solution to the problem. Moreover, the parameter values based on those of Ref. [35] are shown in Table 3.

Table 3
Gas diffusion layers parameter set

Parameters	Value
ε	0.5
V_{GDL} (m^3)	2.53×10^{-4}
D_v ($m^2\,s^{-1}$)	34.5×10^{-6}
δ_{GDL} (m)	00.5×10^{-3}
γ	0.9×10^{3}
s_{im}	0.1
σ ($N\,m^{-1}$)	0.5
θ_c (°)	120
μ (m^2)	2.55×10^{-13}
η_l ($kg\,(m\,s)^{-1}$)	978

The equations that model all the phenomena occurring inside the layers can be divided into two groups: gaseous phase and liquid phase. As nitrogen is an inert gas, it will not be taken into account. Also, oxygen and hydrogen inside the GDLs will be assumed to be at the same pressure as they are in the flow channels. Therefore, the hydrogen and oxygen flow between the channels and the diffusion layers will be imposed by the electrochemical reaction. Thus, the mathematical formulation is then simplified, modeling the water steam concentration gradients, the liquid water capillary pressure and the water condensation dynamics.

3.1.3.1. Gas phase. Gaseous species diffusion occurs between low concentration regions and higher concentration ones. Hence, water steam molar concentrations inside each diffusion gas layers are calculated as

$$c_{v,caGDL} = \frac{p_{v,caGDL}}{RT_{st}} \quad (32)$$

$$c_{v,cach} = \frac{p_{v,cach}}{RT_{st}} \quad (33)$$

$$c_{v,anGDL} = \frac{p_{v,anGDL}}{RT_{st}} \quad (34)$$

$$c_{v,anch} = \frac{p_{v,anch}}{RT_{st}} \quad (35)$$

The effective diffusion rate, $\langle D_j \rangle$, is a function of the gas diffusion layer porosity [35], $\varepsilon = V_p\, V_{GDL}^{-1}$, the fraction of liquid water volume to the total volume s, and the diffusion coefficient D_j:

$$s_j = \frac{V_{l,j}}{V_p} \quad \text{for} \quad j = \text{caGDL,anGDL} \quad (36)$$

$$\langle D_{v,ca} \rangle = D_v \varepsilon \left(\frac{\varepsilon - 0.11}{1 - 0.11}\right)^{0.785} (1 - s_{ca})^2 \quad (37)$$

$$\langle D_{v,an} \rangle = D_v \varepsilon \left(\frac{\varepsilon - 0.11}{1 - 0.11}\right)^{0.785} (1 - s_{an})^2 \quad (38)$$

Molar flows are a function of the effective diffusivity and concentration gradients:

$$N_{\mathrm{v,ca}} = -\langle D_{\mathrm{v,ca}}\rangle \left(\frac{c_{\mathrm{v,cach}} - c_{\mathrm{v,caGDL}}}{\delta_{\mathrm{GDL}}}\right) \tag{39}$$

$$N_{\mathrm{v,an}} = \langle D_{\mathrm{v,an}}\rangle \left(\frac{c_{\mathrm{v,anch}} - c_{\mathrm{v,anGDL}}}{\delta_{\mathrm{GDL}}}\right) \tag{40}$$

where δ_{GDL} is the diffusion layer thickness.

Water steam partial pressures inside the diffusion layers are evaluated as

$$\frac{\mathrm{d}p_{\mathrm{v,caGDL}}}{\mathrm{d}t} = RT_{\mathrm{st}}\left(\frac{N_{\mathrm{v,gen}} + N_{\mathrm{v,memb}} - N_{\mathrm{v,ca}}}{\delta_{\mathrm{GDL}}} + R_{\mathrm{evap,ca}}\right) \tag{41}$$

$$\frac{\mathrm{d}p_{\mathrm{v,anGDL}}}{\mathrm{d}t} = RT_{\mathrm{st}}\left(\frac{N_{\mathrm{v,an}} - N_{\mathrm{v,memb}}}{\delta_{\mathrm{GDL}}} + R_{\mathrm{evap,an}}\right) \tag{42}$$

where $N_{\mathrm{v,memb}}$ is calculated in Section 3.1.4

Evaporation flows are modeled as presented by [35]:

$$R_{\mathrm{evap,ca}} = \gamma\frac{p_{\mathrm{sat}}(T_{\mathrm{st}}) - p_{\mathrm{v,caGDL}}}{RT_{\mathrm{st}}} \tag{43}$$

$$R_{\mathrm{evap,an}} = \gamma\frac{p_{\mathrm{sat}}(T_{\mathrm{st}}) - p_{\mathrm{v,anGDL}}}{RT_{\mathrm{st}}} \tag{44}$$

where, with j = ca,an, a constraint to prevent the evaporation of more liquid water than is available must be included:

$$\text{if } V_{\mathrm{l},j} = 0 \quad \text{and} \quad R_{\mathrm{evap},j} > 0 \Rightarrow R_{\mathrm{evap},j} = 0. \tag{45}$$

Lastly, oxygen and hydrogen flows and the amount of water steam generated in the electrochemical reaction are calculated using stoichiometric balances:

$$N_{\mathrm{v,gen}} = \frac{I_{\mathrm{st}}}{2FA_{\mathrm{fc}}} \tag{46}$$

$$N_{\mathrm{O_2,react}} = \frac{I_{\mathrm{st}}}{4FA_{\mathrm{fc}}} \tag{47}$$

$$N_{\mathrm{H_2,react}} = \frac{I_{\mathrm{st}}}{2FA_{\mathrm{fc}}} \tag{48}$$

F being the Faraday constant.

Mass gaseous flows exchanged between gas diffusion layers and flow channels are calculated below:

$$\dot{m}_{\mathrm{H_2,anGDL2anch}} = A_{\mathrm{fc}}n_{\mathrm{fc}}M_{\mathrm{H_2}}N_{\mathrm{H_2,react}} \tag{49}$$

$$\dot{m}_{\mathrm{O_2,caGDL2cach}} = A_{\mathrm{fc}}n_{\mathrm{fc}}M_{\mathrm{O_2}}N_{\mathrm{O_2,react}} \tag{50}$$

$$\dot{m}_{\mathrm{v,anGDL2anch}} = A_{\mathrm{fc}}n_{\mathrm{fc}}M_{\mathrm{v}}N_{\mathrm{v,an}} \tag{51}$$

$$\dot{m}_{\mathrm{v,caGDL2cach}} = A_{\mathrm{fc}}n_{\mathrm{fc}}M_{\mathrm{v}}N_{\mathrm{v,ca}}. \tag{52}$$

3.1.3.2. Liquid phase. Liquid water volume evaluation is based on mass balances in both the anode and the cathode sides, as

$$\rho_{\mathrm{l}}\frac{\mathrm{d}V_{\mathrm{l,caGDL}}}{\mathrm{d}t} = -\dot{m}_{\mathrm{l,caGDL2cach}} - R_{\mathrm{evap,ca}}M_{\mathrm{v}}\varepsilon V_{\mathrm{GDL}} \tag{53}$$

Table 4
Membrane parameter set

Parameters	Value
α_{w}	15
δ_{memb} (m)	35×10^{-6}
$\rho_{\mathrm{memb,dry}}$ (kg m^{-3})	2×10^{3}
$M_{\mathrm{memb,dry}}$ (kg mol^{-1})	1.1

$$\rho_{\mathrm{l}}\frac{\mathrm{d}V_{\mathrm{l,anGDL}}}{\mathrm{d}t} = \dot{m}_{\mathrm{l,anGDL2anch}} - R_{\mathrm{evap,an}}M_{\mathrm{v}}\varepsilon V_{\mathrm{GDL}} \tag{54}$$

where ρ_{l} is the liquid water density.

Let j = ca,an. The reduced liquid water saturation $S_{\mathrm{r},j}$, s_{im} being the liquid water immobile saturation [35], is modeled as

$$S_{\mathrm{r},j} = \begin{cases} \dfrac{s_j - s_{\mathrm{im}}}{1 - s_{\mathrm{im}}} & \text{para } s_{\mathrm{im}} < s_j \le 1 \\ 0 & \text{para } 0 \le s_j \le s_{\mathrm{im}} \end{cases} \tag{55}$$

Furthermore, the capillary pressure ρ_{c} is calculated via the Leverette J function, which describes the relationship between the capillary pressure and the reduced liquid water saturation S_{r}.

$$\rho_{\mathrm{c}} = \frac{\sigma\cos\theta_{\mathrm{c}}}{(K/\varepsilon)^{1/2}}\underbrace{[1.417S_{\mathrm{r}} - 2.120S_{\mathrm{r}}^2 + 1.263S_{\mathrm{r}}^3]}_{J(S_{\mathrm{r}})} \tag{56}$$

where σ is the surface tension which corresponds to water and air, θ_{c} is the contact angle and μ is the absolute permeability.

At this point, the capillary flows of liquid water $\dot{m}_{\mathrm{l,caGDL2cach}}$ and $\dot{m}_{\mathrm{l,anGDL2anch}}$ can then be defined as in Refs. [35,37], where $\mu_{\mathrm{rl}} = S_{\mathrm{r}}^3$ is the relative permeability of liquid water and η_{l} is its viscosity:

$$\dot{m}_{\mathrm{l,caGDL2cach}} = \frac{A_{\mathrm{fc}}n_{\mathrm{fc}}\mu\mu_{\mathrm{rl}}}{\eta_{\mathrm{l}}}\left|\frac{\mathrm{d}\rho_{\mathrm{c}}}{\mathrm{d}S}\right|\frac{S_{\mathrm{ca}}}{\delta_{\mathrm{GDL}}} \tag{57}$$

$$\dot{m}_{\mathrm{l,anGDL2anch}} = -\frac{A_{\mathrm{fc}}n_{\mathrm{fc}}\mu\mu_{\mathrm{rl}}}{\eta_{\mathrm{l}}}\left|\frac{\mathrm{d}\rho_{\mathrm{c}}}{\mathrm{d}S}\right|\frac{S_{\mathrm{an}}}{\delta_{\mathrm{GDL}}}. \tag{58}$$

3.1.4. Membrane

As the equations presented in this section are analogous to the ones published in Ref. [26], the main innovation regarding the membrane is the parameter adaptation for the Ballard stack, which is presented in Table 4.

The membrane, being waterproof, does not allow the circulation of liquid water but does permit gas diffusion. Therefore, oxygen, hydrogen, nitrogen and water steam are exchanged between both sides of the membrane. As the anode is fed with pure hydrogen, nitrogen flow occurs in the direction of the anode. This phenomenon is negligible due to its very slow dynamics and also because nitrogen is an inert gas that does not affect the electrochemical reaction. Moreover, the amount of nitrogen inside the anode will never be significant, as it is dragged during purging. Water steam flow is a more complex issue as it is a convergence of two distinct phenomena: 'electro-osmotic drag' and 'back diffusion'. Thus, the molar flow across the membrane, published by Springer et al. [38], is described as

$$N_{\mathrm{v,memb}} = n_{\mathrm{d}}\frac{j}{F} - \alpha_{\mathrm{w}}D_{\mathrm{w}}\frac{c_{\mathrm{v,ca}} - c_{\mathrm{v,an}}}{\delta_{\mathrm{memb}}} \tag{59}$$

where $j = I_{st}/A_{fc}$ is the current density, n_d the electro-osmotic drag coefficient, D_w the mass diffusivity of water vapor in the membrane, δ_{memb} the membrane thickness and $c_{v,ca}$ and $c_{v,an}$ are the water concentrations in both sides of the membrane. α_w is an experimental parameter which corrects the possible deviations of the experimental values obtained from the literature, as they might be obsolete due to their being based on older membranes.

The concentrations $c_{v,j}$, where the subscript j corresponds to both the cathode and the anode, are calculated as

$$c_{v,j} = \frac{\rho_{memb,dry}}{M_{memb,dry}} \lambda_j \tag{60}$$

where $\rho_{memb,dry}$ is the dry membrane density, $M_{memb,dry}$ the dry membrane molecular weight and λ_j is calculated as

$$\lambda_j = 0.043 + 17.81a_j - 39.85a_j^2 + 36.0a_j^3 \tag{61}$$

a_j being equal to ϕ_{jGDL}, the relative humidity of the gas inside the gas diffusion layers.

D_w is calculated as the piece-wise linear approximation shown below:

$$D_w = D_{\lambda_{an}} \exp\left(2416\left(\frac{1}{303} - \frac{1}{T_{st}}\right)\right) \tag{62}$$

$$D_{\lambda_{an}} = \begin{cases} 10^{-10}, & \lambda_{an} < 2 \\ 10^{-10}(1 + 2(\lambda_{an} - 2)), & 2 \le \lambda \le 3 \\ 10^{-10}(3 - 1.67(\lambda_{an} - 3)), & 3 < \lambda < 4.5 \\ 1.25 \times 10^{-10}, & \lambda_{an} \ge 4.5 \end{cases} \tag{63}$$

where j corresponds to an,ca and $D_{\lambda_{an}}$ is the corrected diffusivity coefficient. Lastly, the electro-osmotic drag coefficient, described by Dutta et al. [15], is calculated using:

$$n_d = 0.0029\lambda_{an}^2 + 0.05\lambda_{an} - 3.4 \times 10^{-19}. \tag{64}$$

3.2. Electrochemical equations

This section presents one of the main contributions of this paper. In fact, in the mathematical description of the polarization curve, despite being based on the same general equation as the one extensively used in the literature (see Eq. (65)), all of the equation terms are presented in a novel way, thereby optimizing and simplifying its formulation. As a result, a direct algebraic algorithm can be geometrically deduced, in order to adapt the polarization curve so that it corresponds to the experimental data associated with a given PEM stack. All of these parameters, which are obtained below in this section for the Ballard stack, are shown in Table 5:

$$V_{fc} = v_0 - v_{act} - v_{ohm} - v_{conc}. \tag{65}$$

The voltage supplied is evaluated by curves that present the voltage of the cell versus the current density, $j = I_{st}/A_{fc}$. Fig. 3 shows different real voltage data corresponding to several values of temperature, oxygen partial pressure and current density taken from the Ballard stack, while the hydrogen partial pressure was maintained nearly constant and equal to 1.25 bar. Notice that the upper graph shows voltage data for different current density values, while the middle graph presents the temperature of the stack for each experimental point. Lastly, the lower graph shows the calculated oxygen partial pressure corresponding to each value. The main factors that influence the polarization curves are:

Table 5
Electrochemical parameter set

Parameters	Value
(p_{1i}, p_{1v})	(0, 1)
(p_{2i}, p_{2v})	(0.06, 0.785)
(p_{3i}, p_{3v})	(0.4, 0.555)
(p_{4i}, p_{4v})	(0.5, 0.35)
$p^0_{O_2,ca}$	0.16 (bar)
$p^0_{H_2,an}$	1.25 (bar)
T^0_{st}	308 (K)
$\frac{\Delta V_{fc}}{\Delta T_{st}}$	2.93×10^{-3} (V K^{-1})
$\frac{\Delta V_{fc}}{\Delta p_{O_2,ca}}$	7.61×10^{-1} (V bar^{-1})
$(x_1, x_2, x_3, x_4, x_5, x_6, x_7, x_8)$	(1.17, 7.61×10^{-3}, 0.24, 0.18, 1.50×10^{-2}, 0.64, 288.59, 10.00)
α_1	15

- *Current*: open circuit voltage (v_0) falls as the current supplied by the stack increases. Thus, in the first stage, up to a certain current value, activation overvoltage drops (v_{act}) prevail, as a result of the need to move electrons and to break and form chemical bonds. At a later stage, as current density rises, ohmic losses (v_{ohm}) prevail. They are derived from membrane resistance to transfer protons and from electrical resistance of the electrodes to transfer electrons. When current is very high, at maximum power level, concentration overvoltage (v_{conc}) produces a quick drop of the voltage due to internal inefficiencies at high levels of reactives consumption. Although these last drops are modeled by the equation proposed here, such high current values are not normal as they can cause fast degradation of the membranes of the cells. In Fig. 4, the polarization curve that corresponds to the 1.2 kW stack modeled

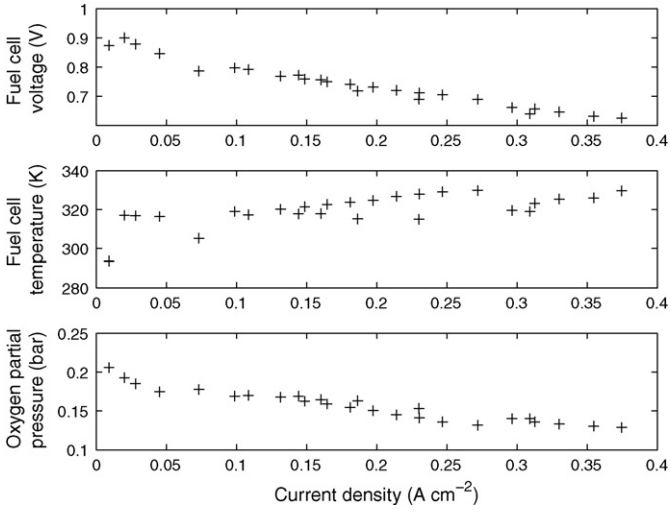

Fig. 3. Experimental data for several partial pressures and temperatures.

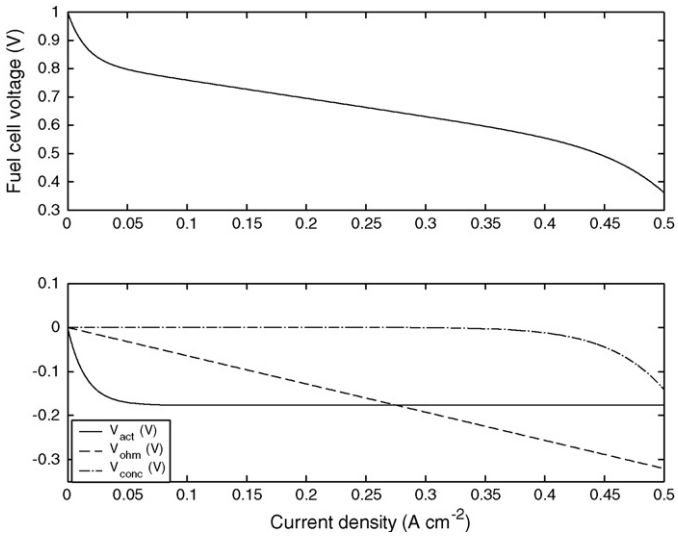

Fig. 4. Fuel cell polarization curve and voltage drops contributions.

here can be seen. The drops described above are case-adapted as well.

- *Reactant partial pressures variances*: oxygen partial pressure inside the cathode and hydrogen partial pressure inside the anode notably influence the voltage supplied by the fuel cells. As the pressure of any of these gases rises, the voltage increases for every current level. Due to the typical dead-end configuration of fuel cell stacks system, hydrogen partial pressure inside the anode remains nearly constant. Thus, the oxygen partial pressure is that which fluctuates more during power demand changes, as it depends on auxiliary equipment dynamics. The oxygen influence can be seen in Fig. 5. The surface shown was obtained solving the equations proposed and plotting the polarization curves corresponding to values of oxygen partial pressure ranging from 0 to 0.25 bar, while maintaining the stack temperature and the hydrogen partial pressure constant at 310 K and 1.25 bar, respectively. Also, experimental data was included, thus comparing theoretical and measured values. Notice the logarithmical tendency of the curves, which is described below in this section, particularly at low oxygen partial pressures, allowing the fuel cell system start-up sequence to be modeled (see also Fig. 8).

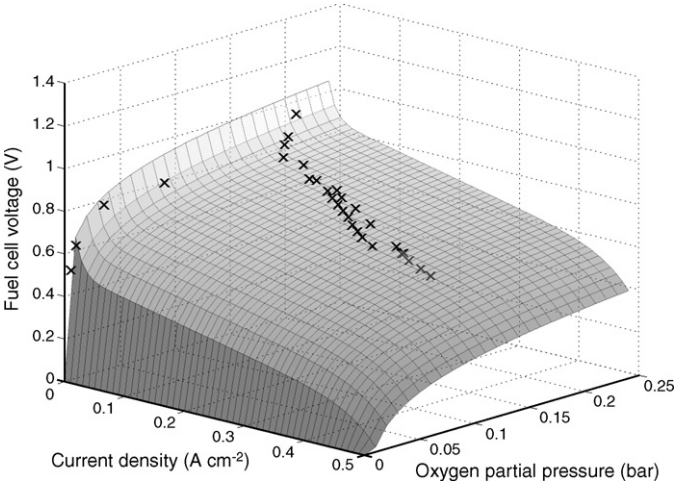

Fig. 5. Oxygen partial pressure influence on the calculated polarization curve and experimental data (*x*).

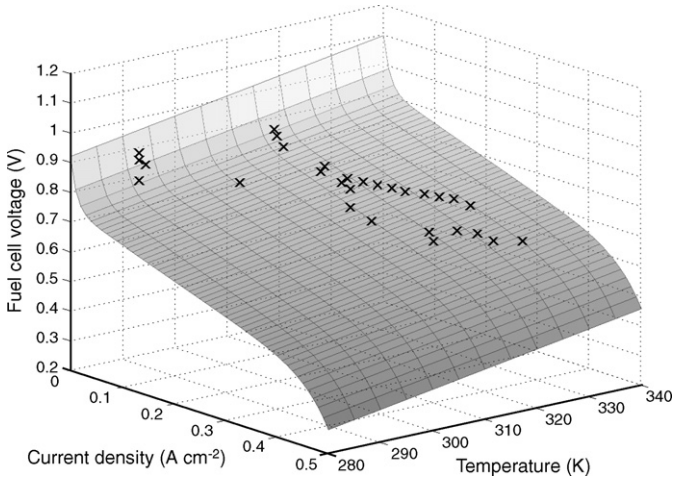

Fig. 6. Temperature influence on the calculated polarization curve and experimental data (*x*).

- *Temperature*: fuel cell stack temperature has many effects on fuel cell performance, including changing the activity of the catalyst, the membrane humidification state, the saturation in GDLs and gas diffusion. For purposes of simplification, we will assume that, on one hand, temperature changes affect the gas pressure inside both anode and cathode. On the other hand, membrane characteristics change as the temperature rises, which results in a voltage increase at every current level. As a result, it is important to distinguish between these two effects when realizing an experimental characterization of the fuel cells. Due to the technical constraint of including pressure sensors inside the flow channels, mathematical modeling is important to obtain simulated values of these pressures, as well as to discriminate the two effects described above. Fig. 6 shows the calculated polarization curve and its dependency on temperature (ranging from 280 to 340 K), maintaining the oxygen partial pressure at a constant value of 0.15 bar and the hydrogen partial pressure at a value of 1.25 bar. Experimental data was included to show the accuracy of the theoretical model proposed here.
- *Amount of condensed water*: liquid water occupies pore volume and reduces the gas diffusion layer surface resulting in voltage and fuel cell efficiency drops. This phenomenon is not important in the cathode side as the water excess is dragged by the air flow, but water accumulates in the anode side until it is dragged during a purge event. This effect has been modeled around the assumption that as the amount of liquid water inside the diffusion gas layer increases, the membrane effective area decreases, resulting in an increased current density and hence a drop in voltage, as shown in Fig. 7, where the calculated current density $j = I_{st}/A_{fc,effective}$ from the measured value of I_{st} and the calculated value of $A_{fc,effective}$ is presented in the upper graph, while the measured and calculated voltages are plotted in the lower graph. Some papers, such as in Ref.

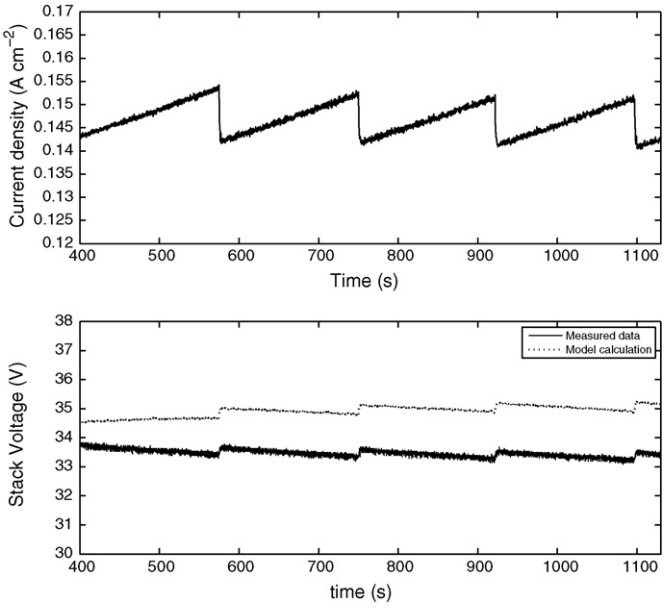

Fig. 7. Current density during purge events.

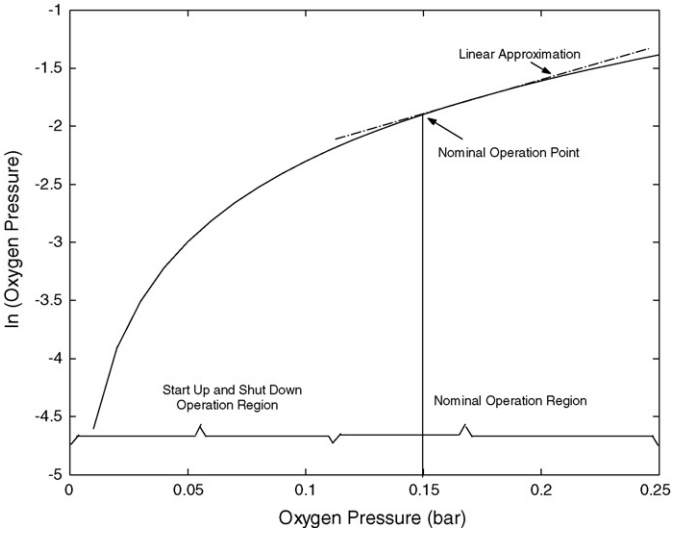

Fig. 8. Oxygen pressure in different operation ranges.

[26], present also the same approach, as under testing conditions, they have proven experimentally that cathode purges have little effect on cell voltages. At the same time, they found that voltage significantly recovered following an anode purge. This phenomenon can be explained since the liquid water condensed in the cathode side is continuously dragged by the exhaust air crossing the cathode. As the anode is in dead-end mode, the liquid water accumulated is not dragged, except after purges. Also, as discussed in Ref. [26], this water forms a thin film (experimentally measured in Ref. [39]) blocking part of the active fuel cell area (resulting in a lower apparent active fuel cell area value $A_{\text{fc,effective}}$) and thus increasing the current density.

Thus, the following equation is proposed to model all the aspects described above:

$$V_{\text{fc}} = \underbrace{x_1}_{v_0} + \underbrace{x_2(T_{\text{st}} - T_{\text{st}}^0)}_{\Delta V_{\text{fc}}/\Delta T_{\text{st}}} + \underbrace{x_3(0.5\ \ln(p_{\text{O}_2,\text{ca}}) + \ln(p_{\text{H}_2}))}_{\Delta V_{\text{fc}}/\Delta p} - \underbrace{x_4(1 - \exp(-j/x_5))}_{v_{\text{act}}} - \underbrace{x_6 \cdot j}_{v_{\text{ohm}}} - \underbrace{x_7 \cdot j^{(1+x_8)}}_{v_{\text{conc}}} \quad (66)$$

$$j = \frac{I_{\text{st}}}{A_{\text{fc}}} = \frac{I_{\text{st}}}{\underbrace{A_{\text{fc}}^0(1 - \alpha_{\text{l}} m_{\text{l,anch}})}_{A_{\text{fc effective}}}}. \quad (67)$$

The logical constraint of V_{fc} being positive or zero, must be included with the stack voltage, being defined as the sum of all individual cell voltages:

$$V_{\text{fc}} \geq 0 \quad (68)$$

$$V_{\text{st}} = n_{\text{fc}} V_{\text{fc}}. \quad (69)$$

The assumptions made in order to obtain the electrical equation are:

- Distinction between temperature and oxygen and hydrogen pressure influences.
- Linear voltage variations near a nominal temperature T_{st}^0. This does not imply less generality as it can be experimentally proven that linear range covers almost all the normal operational range of the stack.
- Logarithmic voltage variations as reactant partial pressures change. This allows the start-up sequence modeling. However, notice that linearity can be assumed near the nominal points $p_{\text{O}_2,\text{ca}}^0$ and $p_{\text{H}_2,\text{an}}^0$. On one hand, this assumption makes the determination of $\Delta V_{\text{fc}}/\Delta p_{\text{O}_2,\text{ca}}$ much easier. On the other hand, it simplifies the algebraic algorithm used to obtain the parameters. The logarithmic tendency is more important during start up and shut down stages, when reactant partial pressures are outside of the nominal operational range (see Fig. 8).

The purpose of the algebraic algorithm presented below is the calculation of the parameters $x_1, \ldots, x_8$. Four experimental points, (p_{ji}, p_{jv}) for $j = 1, \ldots, 4$, which define the shape of the polarization curve, are necessary. Also, the coefficients $\Delta V_{\text{fc}}/\Delta T_{\text{st}}$ and $\Delta V_{\text{fc}}/\Delta p_{\text{O}_2,\text{ca}}$ must be known. The four points must be chosen as they divide the polarization curve into three parts, each one corresponding to one of the three voltage drops described at the beginning of this section. Also, $\Delta V_{\text{fc}}/\Delta T_{\text{st}}$ and $\Delta V_{\text{fc}}/\Delta p_{\text{O}_2,\text{ca}}$ are experimentally obtained from the operation of the fuel cell stack near the nominal points T_{st}^0 and $p_{\text{O}_2,\text{ca}}^0$ respectively. In this way, and after scaling the experimental data shown in Fig. 3 using the values $\Delta V_{\text{fc}}/\Delta T_{\text{st}}$ and $\Delta V_{\text{fc}}/\Delta p_{\text{O}_2,\text{ca}}$, a polarization curve at a fixed temperature (308 K) and oxygen (0.16 bar) and hydrogen (1.250 bar) partial pressures is obtained. In Fig. 9 an example of a possible choice of the four points needed by the algorithm is shown. Also, the experimental data were collected after a purge event, so the measurements were not

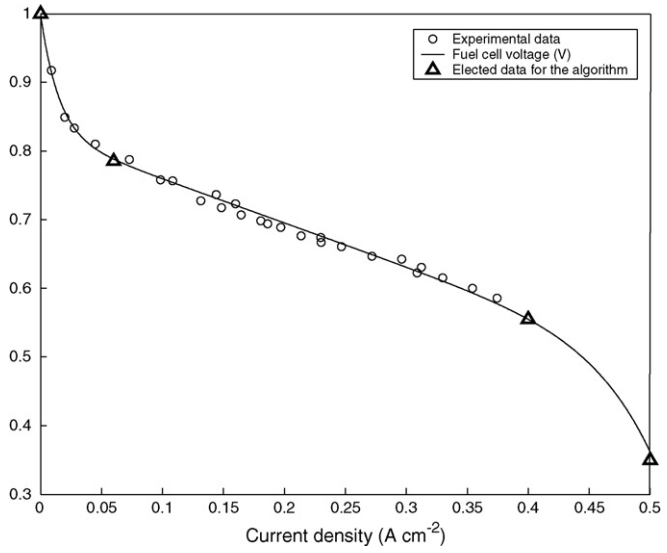

Fig. 9. Point choice for the parameter identification algorithm of the polarization curve.

affected by the flooding effect. Comparing Figs. 3 and 9, data alignment can be observed. Notice that this can be taken as an experimental verification of all the assumptions of linearity and distinction between temperature and reactant partial pressures discussed above:

$$x_8 = \frac{1 + p_{4i}^2}{0.25 p_{4i}} \tag{70}$$

$$x_7 = \frac{(p_{4v} - p_{3v}) + (p_{2v} - p_{3v})((p_{4i} - p_{3i})/(p_{3i} - p_{2i}))}{-p_{4i}^{(1+x_8)} + p_{3i}^{(1+x_8)}((p_{4i} - p_{3i})/(p_{3i} - p_{2i}))} \tag{71}$$

$$x_6 = \frac{(p_{2v} - p_{3v}) - x_7 p_{3i}^{(1+x_8)}}{(p_{3i} - p_{2i})} \tag{72}$$

$$x_5 = \frac{p_{2i} - p_{1i}}{4} \tag{73}$$

$$x_4 = p_{1v} - p_{2v} - x_6 p_{2i} \tag{74}$$

$$x_3 = 2 p_{O_2,ca}^0 \frac{\Delta V_{fc}}{\Delta p_{O_2,ca}} \tag{75}$$

$$x_2 = \frac{\Delta V_{fc}}{\Delta T_{st}} \tag{76}$$

$$x_1 = p_{1v} - x_3(0.5 \ln(p_{O_2,ca}^0) + \ln(p_{H_2,an}^0)). \tag{77}$$

Lastly, α_l is obtained measuring the experimental voltage drop that occurs as liquid water accumulates in the anode. Due to the technical constraint of placing a sensor inside the anode to measure the amount of liquid water accumulated there, an estimated value is then necessary, resulting in $\alpha_l = 15$, as shown in Table 5.

3.3. Thermal equations

As published in Ref. [33], a simplified thermal model is proposed here, taking into account only the main terms of the overall energy balance. This assumption results in an easier experimental adjusting of the equation parameters. The contribution of this paper to this field is the adaptation of the equations proposed in Ref. [33], so that then characterize the 1.2 kW Ballard stack. As discussed before, the stack modeled in Ref. [33], as in almost all other literature, corresponds to a water-cooled stack system. Here, however, an air-cooled stack has been modeled, and the physical parameters have been obtained as well (see Table 6).

Table 6
Thermal parameter set

Parameters	Value
m_{st} (kg)	5
C_{st} (J kg^{-1} K^{-1})	1100
ε	0.9
$A_{B2Amb,rad}$ (m^2)	0.1410
$A_{B2Amb,conv}$ (m^2)	0.0720
$A_{B2Amb,conv}$ (m^2)	1.2696
$h_{B2Amb,nat}$ (W kg^{-1})	14
K_{h1}	0.0156
K_{h2}	1

An energy balance is done in order to obtain the thermal model, taking into account the energy produced in the chemical reaction of water formation (which is supposed to be formed as water steam) $\dot{H}_{reac}$, the energy supplied in the form of electricity P_{elec} and the amount of heat evacuated by radiation $\dot{Q}_{rad,B2amb}$ and both natural and forced convection $\dot{Q}_{conv,B2amb}$. Heat removal is completed through forced convection by a small fan. In bigger fuel cell stack systems, where the amount of heat is considerably larger, water cooling is necessary. In those cases, the forced convection term should be substituted by other terms which model heat exchange in cooling fluid. The energy balance results in:

$$m_{st} C_{st} \frac{dT_{st}}{dt} = \dot{H}_{reac} - P_{elect} - \dot{Q}_{rad,B2amb} \tag{78}$$

The enthalpy flow rate, where $h_{f,H_2O(g)}^0$ is the mass specific enthalpy of formation of water steam and c_{p,H_2}, c_{p,O_2} and $c_{p,H_2O(g)}$ are the specific heats of hydrogen, oxygen and water steam respectively, will be:

$$\dot{H}_{reac} = \dot{m}_{H_2,reac} \Delta h_{H_2} + \dot{m}_{O_2,reac} \Delta h_{O_2} - W_{H_2O,gen(g)}(h_{f,H_2O(g)}^0 \Delta h_{H_2O(g)}) \tag{80}$$

$$\Delta h_{H_2} = c_{p,H_2}(T_{anch,in} - T^0) \tag{81}$$

$$\Delta h_{O_2} = c_{p,O_2}(T_{cach,in} - T^0) \tag{82}$$

$$\Delta h_{H_2O(g)} = c_{p,H_2O(g)}(T_{st} - T^0) \tag{83}$$

where T^0 is the reference temperature for the enthalpy.

Energy yielded in the form of electricity is calculated as

$$P_{elec} = V_{st} I_{st} \tag{84}$$

Heat exchanged as radiation, where ε is the emissivity, $\sigma = 5.678 \times 10^{-8}$ W m^{-2} K^{-4}, the Stefan–Boltmann constant and $A_{B2amb,rad}$ is the radiation exchange area, is modelled as shown

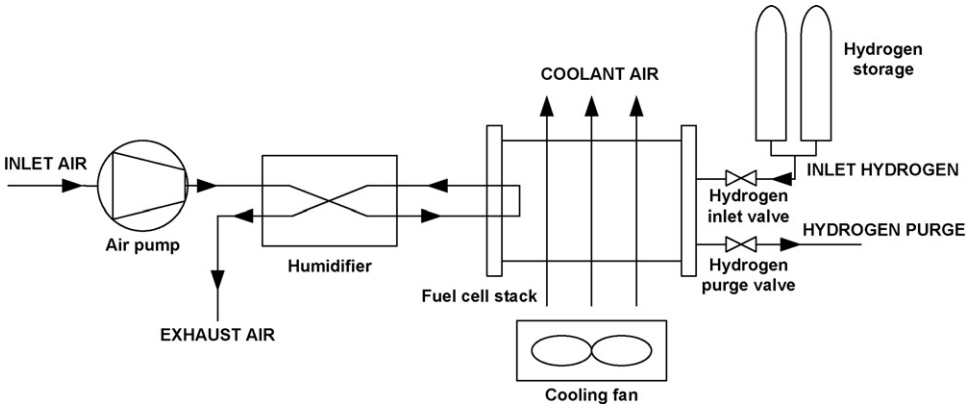

Fig. 10. Nexa power module system.

below:

$$\dot{Q}_{\mathrm{rad,B2amb}} = \varepsilon\sigma A_{\mathrm{B2amb,rad}}(T_{\mathrm{st}}^4 - T_{\mathrm{amb}}^4) \tag{85}$$

Lastly, the convective term is composed by two others, one of them corresponding to the natural convection $\dot{Q}_{\mathrm{conv,B2amb,nat}}$ and the other, to the forced convection $\dot{Q}_{\mathrm{conv,B2amb,forc}}$. In each case, the convective heat transfer coefficients ($h_{\mathrm{B2amb,nat}}$ and $h_{\mathrm{B2amb,forc}}$) are different, just as the exchange areas ($A_{\mathrm{B2amb,conv}}$ and $A_{\mathrm{B2cool,conv}}$) are, because natural convection takes place in the fuel cell lateral walls, and forced convection occurs across the internal walls of the cells, which are constructed as a radiator.

$$\dot{Q}_{\mathrm{conv,B2amb}} = \dot{Q}_{\mathrm{conv,B2amb,nat}} + \dot{Q}_{\mathrm{conv,B2amb,forc}} \tag{86}$$

$$\dot{Q}_{\mathrm{conv,B2amb,nat}} = (h_{\mathrm{B2amb,nat}} A_{\mathrm{B2amb,conv}})(T_{\mathrm{st}} - T_{\mathrm{amb}}) \tag{87}$$

$$\dot{Q}_{\mathrm{conv,B2amb,forc}} = (h_{\mathrm{B2amb,forc}} A_{\mathrm{B2cool,conv}})(T_{\mathrm{st}} - T_{\mathrm{cool}}) \tag{88}$$

where

$$h_{\mathrm{B2amb,forc}} = K_{\mathrm{h1}}(W_{\mathrm{cool}})^{K_{\mathrm{h2}}}. \tag{89}$$

3.4. Auxiliary equipment

Fuel stacks are formed by numerous fuel cells connected in series, but in order to supply energy, they need auxiliary equipment. These devices differ according to the application they are designed for and fuel cell stack size. In this work, a commercial 1.2 kW Nexa module power system is modeled. In Fig. 10, a diagram of the auxiliary equipment can be seen. The devices that are particularized are: air pump, cooling fan, humidifier and inlet hydrogen conditioning system.

3.4.1. Air pump

The air pump is modeled as a black box. Its transfer function, which is identified using experimental data obtained during a test, is presented below. A transfer function is a mathematical representation of the relation between the input and output of a system, and is commonly used in signal processing, communication theory, and control theory. A model with the following discrete time linear transfer function (or transfer operator, see e.g. [40]) is used:

$$y(t) = \frac{0.06229z^2 - 0.0145z}{z^3 - 2.277z^2 + 1.811z - 0.5016}u(t) - 45 \tag{90}$$

where z denotes the shift operator, i.e. $y(t) = y(t-1)z$ and t stands for the current discrete time instant. Here, the model input $u(t)$ is the air pump voltage, which is an analog value ranging from 0% to 100%, corresponding 100% to the maximum air pump power, and the model output $y(t)$ is the air mass flow supplied to the fuel cell stack (kg s^{-1}). In Fig. 11 a comparison between the modeled and the real system can be seen.

3.4.2. Humidifier

Humidifier design is a very complex issue about which there is no available information, as their designers are very confidential regarding new developments. In the model proposed here, the water formed due to the chemical reaction inside the fuel cells is utilized to humidify the inlet air flow. Although some mathematical approaches can be applied, there is insufficient experimental data to validate these models. Thus, it will be assumed that the inlet air flow is optimally humidified after passing across the humidifier, and there is always enough liquid water available

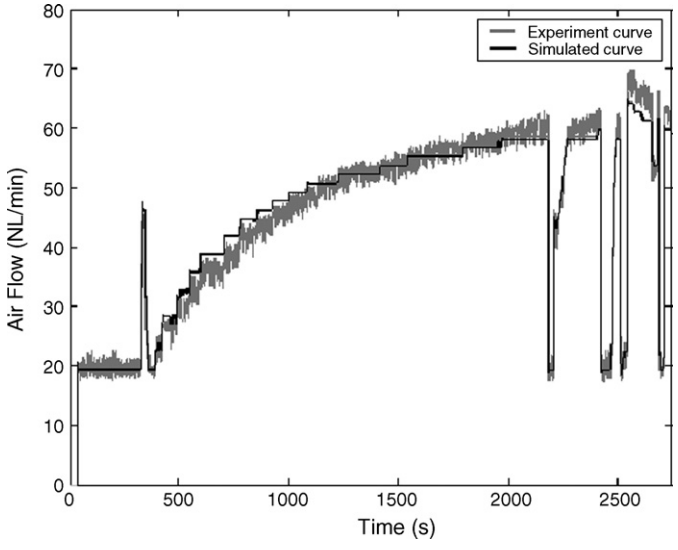

Fig. 11. Air pump real and simulated behavior.

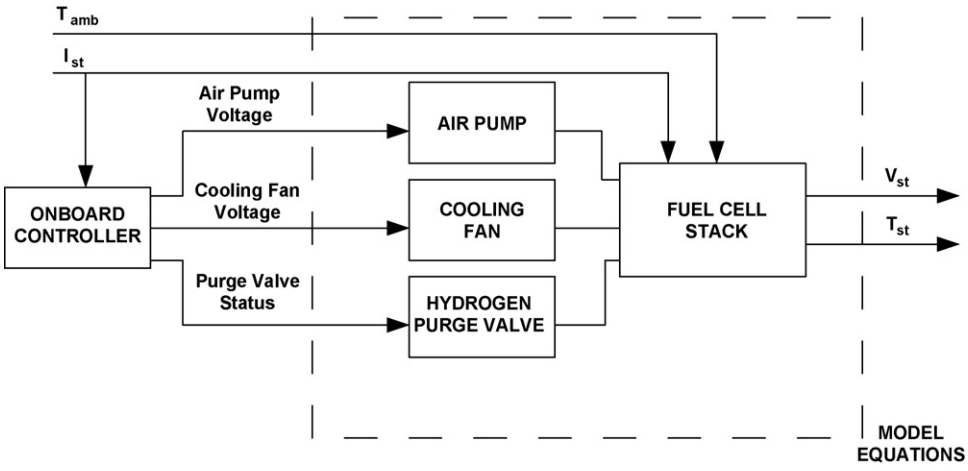

Fig. 12. Model inputs and outputs.

from the chemical reaction. This approximation can be done as it is very close to the real operational conditions.

3.4.3. Cooling fan

In this application, cooling is performed by forced convection. A small fan is used to supply the cooling air flow. The thermal dynamics of the fuel cell are several magnitude orders lower than the fluid-dynamics associated with the cooling air flow, meaning that these dynamics are negligible. Moreover, the amount of air supplied by the fan can be considered as linearly proportional to the control signal of the fan. In this way, the equation that links the model input $u(t)$, which is the fan voltage, between 0% and 100%, with the model output $y(t)$, which is the air flow supplied expressed in kg s^{-1}, is calculated as

$$y(t) = 36u(t). \tag{91}$$

3.4.4. Hydrogen feed system

As can be seen in Fig. 10, the fuel cell system is composed of various pressure regulators and valves that enable or disable the hydrogen supply. The inlet manifold can be modeled as a regulatory valve that adapts the high hydrogen pressure of the tanks to a more suitable and lower pressure inside the anode. Due to this valve, the inlet hydrogen flow equals the hydrogen consumed in the chemical reaction. Thus, $v_{\text{in,open}}$ being equal to 0 when the valve is closed and 1 when it is opened, p_{anch} being the pressure inside the anode, p_{tank} being the tanks pressure, $\dot{m}_{\text{H}_2,\text{an,in}}$ being the hydrogen inlet flow and $K_{\text{an,in}}$ being a characteristic constant of the valve, the model will be:

$$\dot{m}_{\text{H}_2,\text{an,in}} = K_{\text{anch,in}} v_{\text{in,open}}(p_{\text{anch}} - p_{\text{tank}}) \tag{92}$$

In the same way, the purge valve is modeled as

$$\dot{m}_{\text{ma,an,out}} = K_{\text{anch,out}} v_{\text{out,open}}(p_{\text{atm}}). \tag{93}$$

4. Results and discussion

After exposing the model equations, implementing them in Matlab/Simulink and particularizing the physical and experimental parameters of the model to the 1.2 kW Nexa power module, the last step is the model validation. The differential equations have been solved using the ode23s solver method, provided by the cited Matlab/Simulink software package. As have been discussed, the fuel cell stack and its auxiliary devices (which are: air pump, humidifier, cooling fan and hydrogen feed system) have been modeled. Therefore, the inputs to the model are the air pump voltage, the fan voltage, the ambient temperature, the anode purge valve status and the current demanded from the fuel cell system (see Fig. 12). Notice that, depending on the current demand, the onboard controller of the fuel cell system adjusts the air pump and the fan voltages, as well as the hydrogen purge value (which opens to recover the voltage which falls due to the flooding effects). Thus, real data from tests, collected during several experiments, would be the model inputs. The system outputs, which are linked with the inputs through the model equations, are the fuel cell stack voltage and its temperature, and are also measured. The validation process consists of simulating the model applying the real system inputs as model inputs, and then comparing the system outputs with the simulated ones. In this way, four experiments are proposed: start-up stage, constant load (to observe the flooding effect), variable load (to analyze the transitory effects) and a long duration test with load changes (to validate the thermal equations of the model).

4.1. Start-up sequence

During the 'stand by' stage, both the air pump and the cooling fan are off and the hydrogen inlet valve is closed. The period required for nominal conditions to be reached (which happens when the voltage reaches a nominal stationary value), is known as the start-up sequence. When starting up, the air pump and the cooling fan switch on and the hydrogen inlet valve opens. At the same time, the purge valve stays opened (for approximately 15 s) in order to ventilate the anode channel. Notice that, during this time, no current is delivered by the fuel stack, so there is no hydrogen consumption. When a value of approximately 40 V is reached, the start up sequence finishes, and power can then be delivered. As there is no power demand, anode flooding is

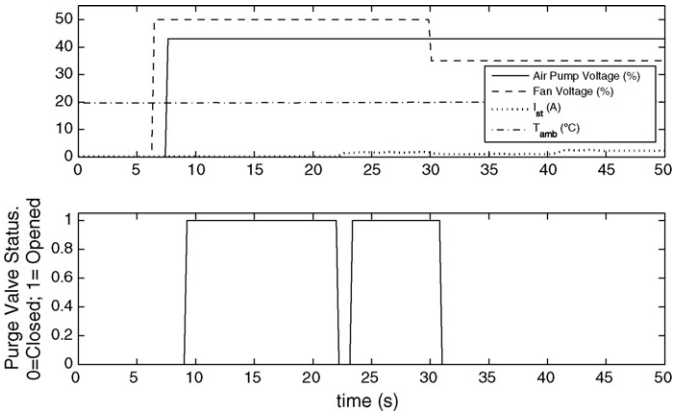

Fig. 13. Input data during the start up sequence.

not serious and therefore cannot be detected when the purge valve opens. Real input and output evolution can be seen in Figs. 13 and 14, as well as the simulated voltage and temperature outputs.

4.2. Constant load: flooding effects

During normal fuel cell operation, liquid water condenses and accumulates in the anode as it is in dead-end mode, decreasing the efficiency and thus requiring anode purges. Thus, the anode outlet valve purges for approximately 2 s. At the same time, as discussed before in this paper, the liquid water accumulated in the cathode is removed continuously by the cathode air exhaust, so there is no need for cathode purges. The experimental data presented was collected applying a constant load, showing the flooding effect as well as the voltage recovery after an anode purge (see Figs. 15 and 16). Notice that when the load changes, as in the other experiments presented in this section, anode flooding occurs as well, but as the voltage drop caused by the flooding is not very high and voltage is continuously changing due to current demand variations, it is difficult to observe flooding effects in those cases. This is the reason why a constant load experiment was performed in order to show the voltage recovery after a purge event.

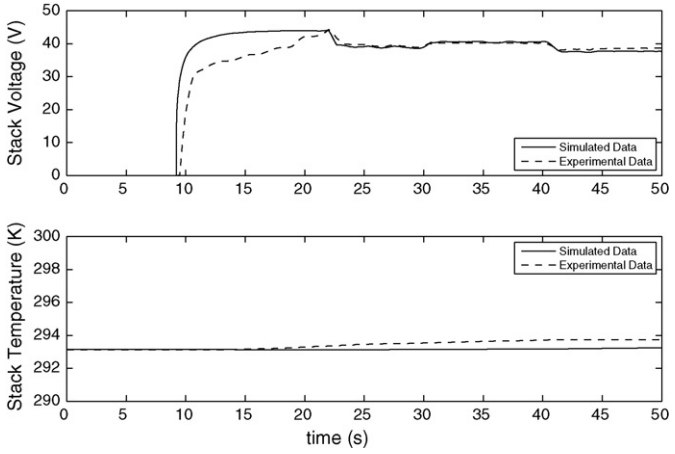

Fig. 14. Output data during the start up sequence.

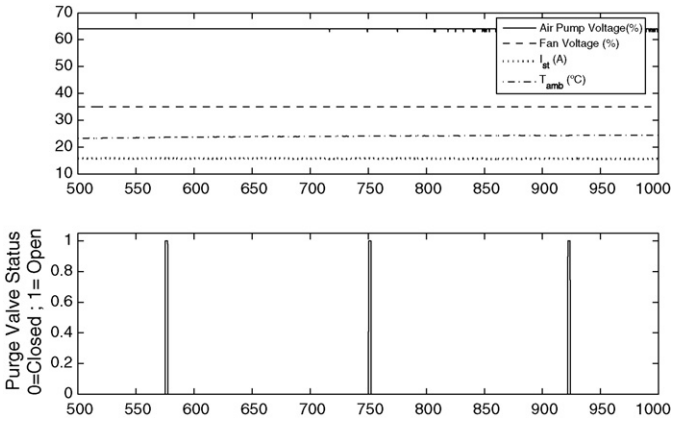

Fig. 15. Input data during flooding test.

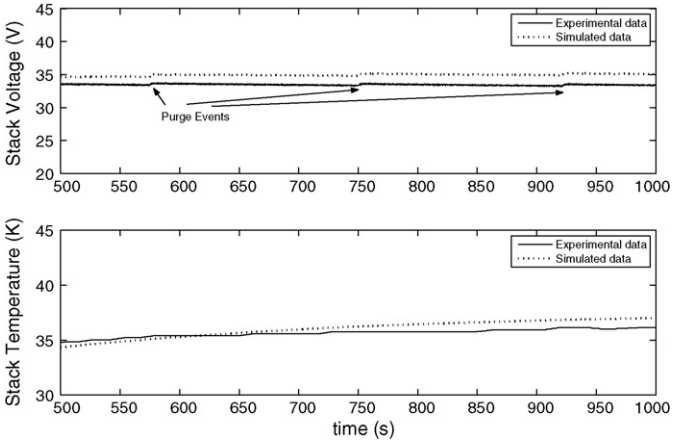

Fig. 16. Output data during flooding test.

4.3. Variable load: transitory effects

During abrupt load changes, the current delivered by the fuel cell stack varies. At that point, the fuel cell system onboard controller adjusts the air pump and the cooling fan voltages, in order to maintain appropriate air feeding and stack temperature, as well as the purge valve, in order to mitigate the flooding effects. These data, including also the ambient temperature, can be seen

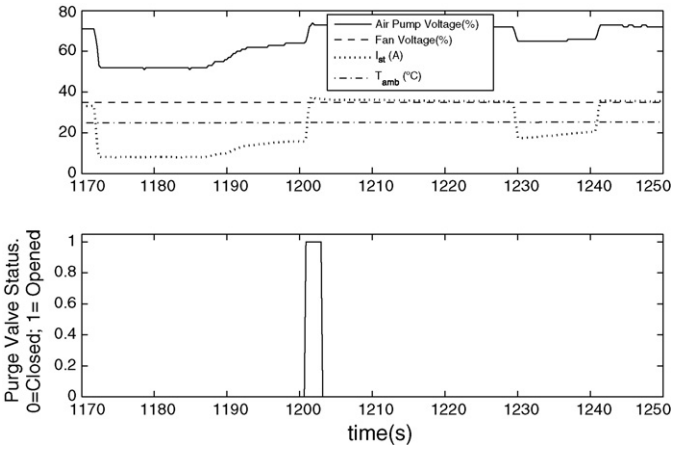

Fig. 17. Input data during transitory effects test.

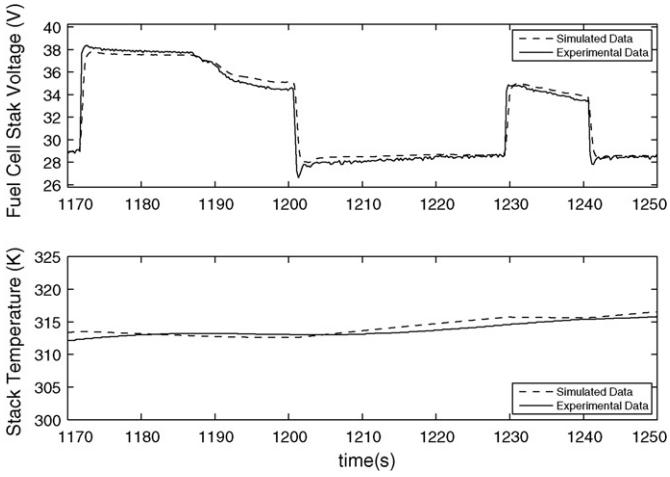

Fig. 18. Output data during transitory effects test.

in Fig. 17, which corresponds to the model inputs. Solving the model equations, the simulated values of voltage and temperature can then be compared with the measured ones, as seen in Fig. 18. Notice that, when the power demand increases, the air supply equipment takes some time to provide the new amount of air required, as the electromechanical dynamics present various orders of magnitude higher than fluid dynamics response time. During this period, the oxygen partial pressure tends to decrease and thus the voltage of the fuel cell stack decreases. Also, during the test, an anode purge can be observed, but notice that, as it was performed during a load change, it is difficult to detect the voltage recovery.

4.4. Variable load: temperature

As thermal effects are much slower than others, a longer test is needed to validate the set of equations dedicated to the stack temperature. In the same fashion as the previous experiments, load changes were applied to the fuel cell system, collecting then the sensor measurements and afterwards, solving the model equations. As can be seen in Figs. 19 and 20, the simulated temperature tracks the real data thoroughly. Also notice that,

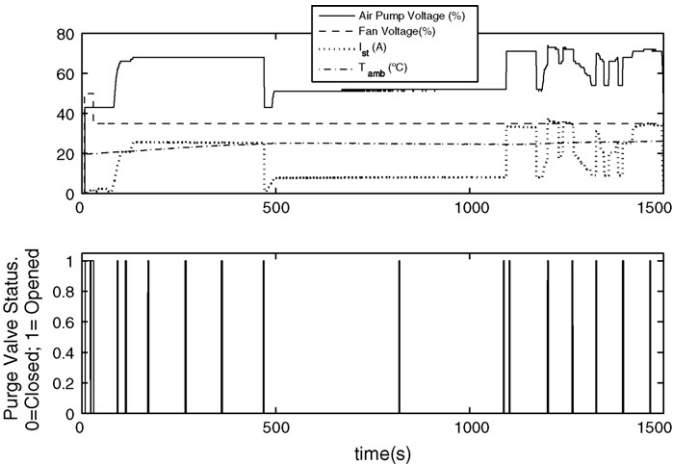

Fig. 19. Input data during thermal effects test.

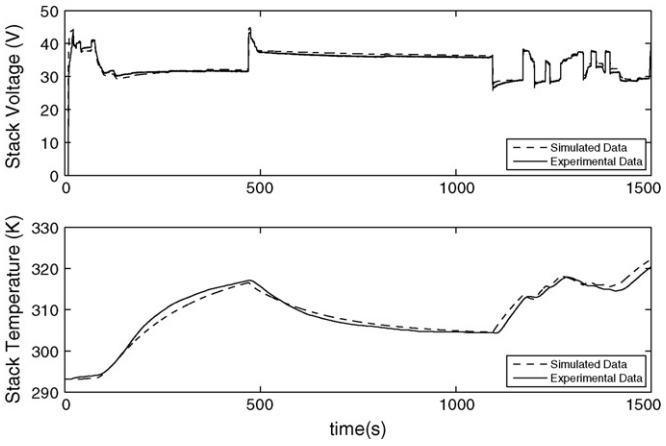

Fig. 20. Output data during thermal effects test.

even when many anode purges are performed, as the graph scale is very large and the voltage recoveries are small, it is difficult to observe them.

5. Conclusions

This work has presented a complete dynamic model of a fuel cell. It is a control-oriented model, that can be used for controller design and optimal operational strategies development for FC-based power systems. The model has been validated on a Ballard 1.2 kW PEM fuel cell which can be considered a benchmark, since it is well-known by many research groups as a good example of the state of the art in this technology. The proposed model's main contributions are related to a novel way of experimentally obtaining the polarization curve, to the adaptation of the thermal equations for an air cooled stack and the modeling of the flooding event. Moreover, the model has been validated on a real plant, showing that simulated data match experimental data quite closely. The simulator software is available upon request.

Acknowledgements

This work was supported by CICYT Contract DPI2004-07444-C04-01. The contribution of Eduardo López from INTA (National Aerospace Institute) is gratefully appreciated. We are also grateful for the comments provided by Anna Stefanopoulou (Department of Mechanical Engineering, University of Michigan).

References

[1] K. Adamson, Energy Policy 32 (2004) 1232–1242.
[2] J. Amphlett, R. Baumert, R. Mann, B. Peppley, P. Roberge, T. Harris, J. Electrochem. Soc. 142 (1995) 9–15.
[3] M.A.S. Al-Baghdadi, Renewable Energy 30 (2005) 1587–1599.
[4] J. Pukrushpan, H. Peng, A. Stefanopoulou, J. Dyn. Syst. Measur. Control 126 (1) (2004) 14–25.
[5] A. Arce, Msc Thesis, University of Seville, 2005.
[6] C. Bordons, A. Arce, A.J. del Real, Proceedings of the 2006 American Control Conference, 2006.
[7] D. Bernardi, M. Vebrunge, J. Electrochem. Soc. 139 (9) (1992) 2477–2491.

[8] T. Springer, T. Zawodzinski, S. Gottesfeld, J. Electrochem. Soc. 138 (8) (1991) 2334–2342.
[9] S. Gurski D. Nelson, Proceedings of the SAE 2003 World Congress and Exhibition, 2003.
[10] F. Buchi, S. Srinivasan, J. Electrochem. Soc. 144 (8) (1997) 2767–2772.
[11] D. Sena, E. Ticianelli, V. Paganin, E. Gonzalez, J. Electroanal. Chem. 477 (1999) 164–170.
[12] T. Fuller, J. Newman, J. Electrochem. Soc. 140 (5) (1993) 1218–1225.
[13] P. Costamagna, Chem. Eng. Sci. 56 (2001) 323–332.
[14] N. Djilali, D. Lu, Int. J. Therm. Sci. 41 (2002) 29–40.
[15] S. Dutta, S. Shimpalee, J.V. Zee, Int. J. Heat Mass Transfer 44 (2001) 2029–2042.
[16] Y. Wang, C. Wang, J. Power Sources 147 (2005) 148–161.
[17] W. Ying, T. Yang, W. Lee, C.K.J. Kea, J. Power Sources 145 (2005) 572–581.
[18] W. Ying, Y. Sohnb, W. Lee, C.K.J. Kea, J. Power Sources 145 (2005) 563–571.
[19] K.W. Luma, J.J. McGuirkb, J. Power Sources 143 (2005) 103–124.
[20] J. Ramousse, J. Deseure, O. Lottin, S. Didierjean, D. Maillet, J. Power Sources 145 (2005) 416–427.
[21] P. Berg, K. Promislow, J.S. Pierre, J. Stumper, J. Electrochem. Soc. 37 (3) (2004) 341–353.
[22] D. Bernardi, M. Verbrugge, AIChE J. 37 (8) (1991) 1151–1163.
[23] T. Fuller, J. Newman, J. Electrochem. Soc. 140 (5) (1993) 1218–1224.
[24] T. Nguyen, R. White, J. Electrochem. Soc. 140 (5) (1993) 2178–2186.
[25] T. Springer, T. Zawodzinski, S. Gottesfeld, J. Electrochem. Soc. 138 (8) (1991) 2334–2342.
[26] D. McKay, W. Ott, A. Stefanopoulou, Proceedings of the ASME International Mechanical Engineering Congress, 2005, IMECE 2005-81484.
[27] K. Promislowa, B. Wettonb, J. Power Sources 150 (2005) 129–135.
[28] J. Koh, A.T. Hsua, M.L.H.U. Akaya, J. Power Sources 144 (2005) 122–128.
[29] X. Yu, B. Zhou, A. Sobiesiak, J. Power Sources 147 (2005) 184–195.
[30] Y. Shan, S.Y. Choe, J. Power Sources 145 (2005) 30–39.
[31] B. Wetton, K. Promislow, A. Caglar, Proceedings of the Second International Conference on Fuel Cell Science, Engineering and Technology, 2004.
[32] M. Sundaresan, PhD Thesis, UC, Davis, 2004.
[33] E.A. Muller, A.G. Stefanopoulou, Proceedings of the Third International Conference on Fuel Cell Science, Engineering and Technology, 2005, FUELCELL2005-74050.
[34] L. Guzzella, NFS Workshop on the Integration of Modeling and Control for Automotive Systems, 1999.
[35] J. Nam, M. Kaviany, Int. J. Heat Mass Transfer 46 (2003) 4595–4611.
[36] M.W. Zemansky, R.H. Dittman, Heat Thermodynamics, McGraw Hill, 1981.
[37] M. Kaviany, Principles of Heat Transfer in Porous Media, 2nd ed., Springer, 1999.
[38] T. Springer, T. Zawoddzinski, S. Gottesfeld, J. Electrochem. Soc. 147 (9) (1991) 1527–1538.
[39] P. Chuang, A. Turhan, A. Heller, J. Brenizer, T. Trabold, M. Mench, Proceedings of the ASME Conference on Fuel Cell Science, Engineering and Technology, 2005.
[40] L. Ljung, System Identification, 2nd ed., Prentice Hall Information and System Sciences Series, New Jersey, 1999.